Materialia 24 (2022) 101506

Contents lists available at ScienceDirect

Materialia

journal homepage: www.elsevier.com/locate/mtla

A modeling approach to predict the mechanical response of materials to irradiation damage from external sources: Nanoindentation of Pb-implanted $ZrSiO_4$

Norbert Huber[a,b,*], Tobias Beirau[c]

[a] Institute of Materials Mechanics, Helmholtz-Zentrum Hereon, Geesthacht 21502, Germany
[b] Institute of Materials Physics and Technology, Hamburg University of Technology (TUHH), Hamburg 21073, Germany
[c] Institute of Geosciences and Geography, Mineralogy/Geochemistry, Martin Luther University, Halle-Wittenberg, Halle 06120, Germany

ARTICLE INFO

Keywords:
Irradiation damage
Amorphization
Nanoindentation
Mechanical properties
Residual stress

ABSTRACT

Materials exposed to external irradiation undergo damage and detoriation of mechanical properties that decays with the distance from the surface. Finite element simulations are used to predict the hardness and Young´s modulus as function of depth. The model incorporates the homogenized mechanical properties and the volumetric swelling, determined from micromechanical simulations, as function of the locally induced damage. Predicted Young's modulus data showed a good agreement with nanoindentation results and confirmed the established mapping of damage into depth dependent amorphous phase fraction in form of sigmoidal functions. The comparison of predicted hardness profiles with experimental data suggests a relaxation mechanism that removes the residual stress in the damaged surface layer during the ion implantation process. Furthermore, the results support the hypothesis that mechanical properties determined from intrinsic damage can be used to model also external radiation damage. The presented model is applicable to other types of materials and irradiation sources.

1. Introduction

The knowledge of the structural and hence mechanical response of materials to external irradiation damage is of high technical and even economic importance to predict the usability and long-term stability under such an extreme condition present in environments with higher radiation levels, e.g., nuclear reactors, nuclear waste storage facilities, earth orbit, space and the moon, and other planets like mars [1–4]. As radiation damage (e.g., induced by elastic collisions between the incoming particle and lattice atoms in its trajectory) can lead to massive structural disorder and finally to an amorphous state, it is crucial to be able to estimate the durability and hence suitability of materials used for operation in enhanced radiation fields (e.g., radiation shielding, technical applications or construction). For this purpose, we extended the modeling approach that has already been successfully used to predict the effect of intrinsic radiation damage on the mechanical properties of ceramic materials [5–7] to also consider the effect of external radiation sources.

Intrinsic structural radiation damage is a volumetric effect that homogeneously changes the material properties on the macroscopic scale. Therefore, as shown by Huber and Beirau, the amorphization and resulting mechanical properties can be modeled on the microstructural length scale via a representative volume element (RVE) and the homogenized mechanical properties can be assigned to the macroscopic sample, e.g., to predict the nanoindentation hardness for a given amorphous fraction [5,6]. In this sense, natural zircon ($ZrSiO_4$) that underwent intrinsic radiation damage is an ideal candidate for model development and validation. The simulation results confirmed the role of the percolation thresholds that emerge for bi-continuous microstructures at ~16 and 84% [8], which reflects in the predicted macroscopic mechanical properties [5,6]. Furthermore, the incorporation of an interface strengthening between the amorphous and the crystalline phase in the RVE allows for reproducing the cusp in the hardness that forms around the percolation threshold at an amorphous fraction of ~16% [5].

The before mentioned technologically highly relevant case of structural damage, caused by external irradiation, leads to a gradual decrease of the damage below the surface. The amount of damage and the penetration depth of the damaged zone increases with the dose. Oliver et al. measured the hardness and modulus for 500 keV $^{208}Pb^{3+}$-ion implanted damage in zircon for doses ranging from 10^{12} to 10^{15} Pb ions/cm^2 [9]. The results showed a softening by 70% and a decrease in modulus by 42% through the crystalline-to-amorphous transition. Because of the sensitivity of hardness and modulus on the indentation depth, substrate-independent values require very shallow indentations. But the measured

* Corresponding author at: Institute of Materials Mechanics, Helmholtz-Zentrum Hereon, Geesthacht 21502, Germany.
E-mail address: norbert.huber@hereon.de (N. Huber).

https://doi.org/10.1016/j.mtla.2022.101506
Received 15 March 2022; Accepted 4 July 2022
Available online 6 July 2022
2589-1529/© 2022 The Author(s). Published by Elsevier B.V. on behalf of Acta Materialia Inc. This is an open access article under the CC BY-NC-ND license (http://creativecommons.org/licenses/by-nc-nd/4.0/)

modulus of the damaged layer is still influenced by the undamaged substrate, even for the shallowest depth of indentation [9].

The work of Huber and Beirau provides a valuable data base and a sufficient extreme case to be used for an extension of the modeling approach, presented in [5], towards predicting the mechanical properties in the course of irradiation damage. With the help of such a model, we provide a possibility to translate a given depth profile, e.g., in the present case the normalized yield measured in [9], into the amorphous phase fraction. The predictions allow to assess if the material properties calibrated for intrinsic damage in [5] can be applied in the same manner also for other types of damage, such as for example ion implantation. For detailed transmission electron microscopy images of externally irradiated zircon it is referred to, e.g., [10,11].

2. Modeling approach

For the simulation of nanoindentation in zircon damaged by ion implantation, we use the FEM mesh that is published in [5,12]. In the earlier work [12], the mesh is split in a film and a substrate for assigning different mechanical properties. Consequently, there is a sharp transition at the interface. For simulation of intrinsically damaged zircon [5], the sample was modeled as bulk material and the homogenized mechanical properties were derived from micromechanical simulations of a bi-continuous microstructure that is generated from leveled-cut random Gaussian fields [8]. This implies two percolation thresholds at phase fractions of $\phi_a^{P1} = 15.9\%$ and $\phi_a^{P2} = 84.1\%$, where ϕ_a is the fraction of the amorphous phase. The first percolation transition at ϕ_a^{P1} characterizes the transition from islands of amorphous zircon within a matrix of crystalline zircon to a bi-continuous network of both phases at lower doses, whereas the second percolation transition ϕ_a^{P2} represents the transition from the bi-continuous network to isolated islands of crystalline phase at higher doses. An interfacial strengthening allows reproducing the measured hardness values between the two percolation thresholds. For details, we refer to [5].

In this work, we will use the data for macroscopic mechanical properties Young's modulus E, Poisson's ratio ν, yield stress σ_y, work hardening rate E_T, and the volumetric swelling V_{sw} as function of the phase fraction ϕ_a, published in [5,7] as initial input for our model. In [5], the true contact area was used to compute the hardness, which avoids uncertainties with possible pile-up behavior [13]. Furthermore, the Young's modulus was determined from uniaxial compression of the micromechanical model and not from the indentation simulation. In the following, we compare the depth dependent hardness and modulus data from [9] with our simulation results, hence the Oliver & Pharr method [14] must be consistently applied. This requires a re-calibration of relevant material parameters.

For the analysis of the simulation results, the rigid indenter is displaced by an indentation depth h at which the hardness $H(A) = P/A$ is computed from the true contact area A, provided by Abaqus as field output variable CAREA [15]. This corresponds to the approach proposed in [5], by which the yield stress has been calibrated for the micromechanical model. Consistent with the experiments [9], the Young's modulus $E(A_c)$ and hardness $H(A_c)$ are now determined following the Oliver & Pharr method [14]. To this end, and in extension of [5], 6 unloadings are inserted in the simulation that correspond to nanoindentation depths of 25, 45, 75, 100, 155, and 255 nm. For a sufficient resolution of the damaged surface relative to the FEM model, which has an edge size of 2 mm, the depth variable in the simulation is scaled by a factor of 1000. Therefore, the maximum indentation depth reaches 10% of the model size and boundary effects require a correction using the method described in [16]. The application of this approach, which corrects the measured stiffness via the solution of a concentrated force acting on an elastic half space after [17], requires the boundaries at the bottom and the side of the model to be fixed.

The correctness of this approach is validated with simulations for bulk materials varying from 0% to 100% damage. From Fig. 1a) can

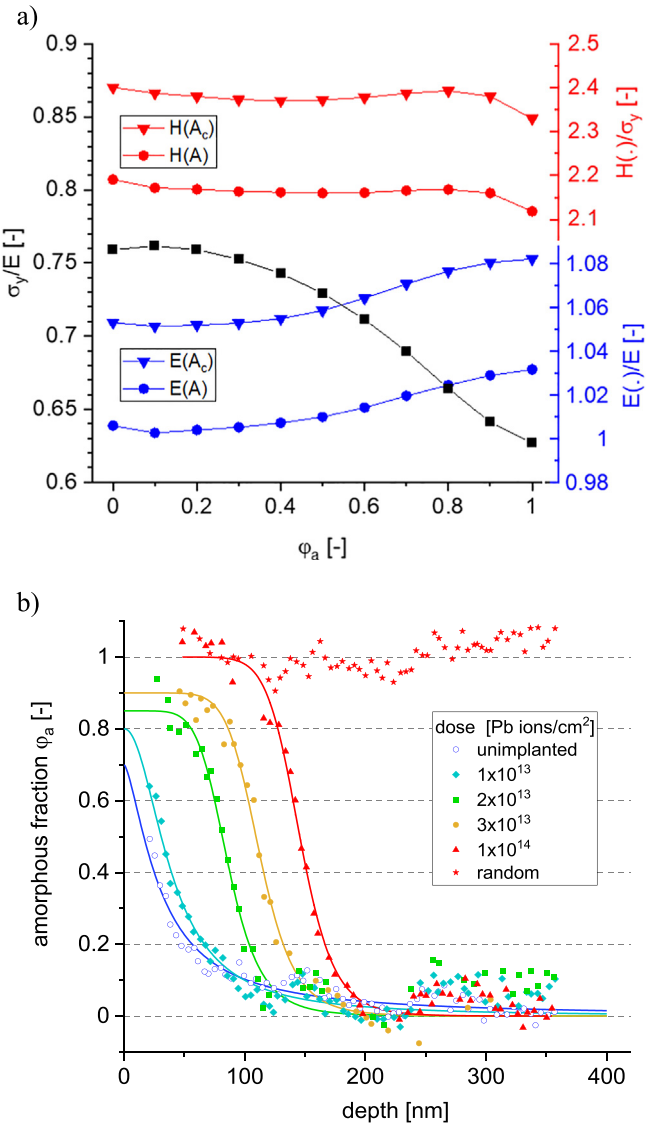

Fig. 1. Input for the simulation model: (a) Effect of the amorphous phase fraction ϕ_a on the mechanical properties in nanoindentation. (b) Data of the energy spectra of 2.0 MeV He ions backscattered from a random orientation (top curve) and the (100) channeling direction [9] mapped to amorphous fraction versus depth.

be seen that the Young's modulus $E(A)$, computed with the true contact area shows only a variation caused by the decay of σ_y/E which remains within 3% error. The Young's modulus $E_{ind}(A_c)$, determined with the Oliver & Pharr method and corrected for the finite boundary effect [16], shows similar variations, but it is slightly higher due to pile-up effects with an average of $E(A_c)/E$ of $1.063 \pm 1.2 \cdot 10^{-2}$. For the hardness to yield stress ratio, we obtain almost perfectly constant values of $H(A)/\sigma_y = 2.162 \pm 1.71 \cdot 10^{-2}$ and $H(A_c)/\sigma_y = 2.377 \pm 1.83 \cdot 10^{-2}$. Therefore, the modulus and hardness as determined with the Oliver & Pharr method is overestimating the true hardness by 6% and 10%, respectively. This is compensated by reducing the corresponding parameters in the model input by the same amount relative to the data provided in [7]. For further details and validation, see Section S1.

Another important input is the depth dependent damage that is induced by the ion implantation. Oliver et al. measured the energy spectra of 2.0 MeV He ions backscattered from a random orientation (top curve) and the (100) channeling direction for synthetic zircon crystals and for natural zircon (Mud Tanks Carbonatite, Northern Territory, Australia)

Table 1
Parameters for the sigmoidal fit of the amorphous fraction ϕ_a, Eq. (1) and Fig. 1b).

Dose(Pb ions/cm^2)	0	$1 \cdot 10^{13}$	$2 \cdot 10^{13}$	$3 \cdot 10^{13}$	$1 \cdot 10^{14}$
$\phi_{max}(-)$	0.7	0.8	0.85	0.9	1.0
h_0(nm)	30.43	39.30	86.14	112.49	145.68
$p(-)$	1.482	2.086	6.374	7.869	10.365

[9]. These spectra provide a measure for the amount of damage that is induced by Pb implantation doses, mapped to normalized damage. The results have in common that the data for unimplanted samples and for the random orientation represent the lower and the upper limit and can therefore be interpreted in sufficient approximation as the boundaries for 0% and 100% amorphization, respectively. The two samples show somewhat different results, i.e., for the synthetic zircon crystals the normalized yield remains fairly constant, whereas for the natural zircon, the data show a linear increase over the depth. This linear increase is removed by a linear fit to the unimplanted data set and, with the same slope, all data of ion implanted samples are corrected. Oliver et al. reported a more pronounced dechanneling at the immediate near-surface that is explained by the mechanical polishing. Therefore, for the fit of the damage with sigmoidal functions, these data points are eliminated. For larger depth, where undamaged material can be assumed, the normalized yield shows a plateau value that increases with the Pb-implantation dose. This plateau value is assigned to a zero damage value for the fit approach. In this way, the normalized yield measured in [9] is mapped to the amorphous phase fraction ϕ_a shown in Fig. 1b). The sigmoidal fits with the function

$$\phi_a = \phi_{max}\left\{1 + \left(\frac{h}{h_0}\right)^p\right\}^{-1} \quad (1)$$

are included as solid curves with the parameters ϕ_{max}, h_0 and p given in Table 1.

For mapping the mechanical properties from the data in Fig. 1b), we assumed that the normalized damage corresponds to the amorphous fraction ϕ_a. A Python script computes the amorphous fraction for all integration points according to their depth position and the fit function shown in Fig. 1b) and stores them as a Fortran data block. Such a data block is included in a user field routine 'usdfldTable[dose].f' assigning the computed amorphous fraction ϕ_a to the integration points of the FEM model via the element and integration point number. Finally, the Abaqus input file contains a material card, which defines the mechanical properties as function of amorphous fraction, defined as field variable SDV1. In this way, the depth dependent damage is efficiently included in Abaqus, while it is ensured that the damage remains constant for a material point, although its vertical coordinate changes during the nanoindentation simulation. Fig. 2 shows an example of an indentation simulation with contour plots of ϕ_a (field variable SDV1) and the Mises stress distribution for the dose of $3 \cdot 10^{13}$ $Pb\,ions/cm^2$.

Concerning the pile-up, which can lead to an underestimation of the true contact area by as much as 60% [13], our analysis shows values for A_c/A of 78%. Although zircon has a high strength and not much pile-up is expected, the squeezing of the softened surface layer leads to a remarkable pile-up and increase of the contact area, as seen in Fig. 2. Similar effects have been observed for Al films on glass [18].

Another important effect is the volumetric swelling that can be expected to cause compressive residual stresses. For investigating this effect, we use the data from [5], where the volumetric swelling as function of the amorphization was predicted. The analysis in Section S2 shows that a swelling strain $\varepsilon_{sw} = 3.78\%$ for fully amorphized material causes an equibiaxial compressive residual stress in the damaged surface that reaches -8.9 GPa in the elastic case. This value exceeds the yield stress of the damaged material and, therefore, the lateral compressive stresses in the surface are limited by the local flow stress of the material. For the simulations, the volumetric swelling is implemented via a thermal expansion in an initial step, where the expansion coefficient, computed from the data provided in [5], is considered as field dependent material parameter as function of the amorphous fraction ϕ_a (SDV1).

3. Results and discussion

Fig. 3 shows the comparison of the predicted hardness and modulus data with the experimental data from [9]. The solid and dashed curves show the results without and with considering swelling and the formation of residual stresses, respectively. For the Young's modulus, shown in Fig. 3a), the overall agreement is very good. For lower doses, the predictions without considering residual stresses seem to fit the experimental data better, whereas for doses $> 2 \cdot 10^{13} Pb\,ions/cm^2$, the residual

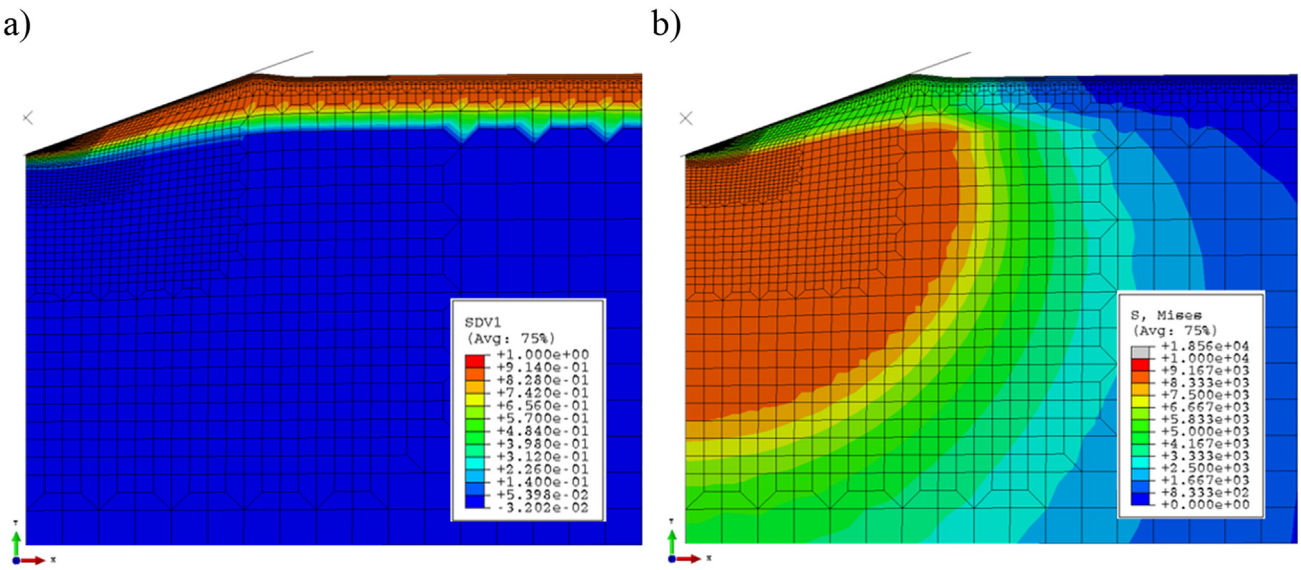

Fig. 2. (a) Damage distribution implemented as user field subroutine shown for a dose of $3 \cdot 10^{13}$Pb ions/cm^2. The damage is assigned via the position of the integration points in the undeformed configuration. (b) von Mises stress distribution revealing the softening of the material in the damaged surface layer, which leads to a pile-up at the contact radius.

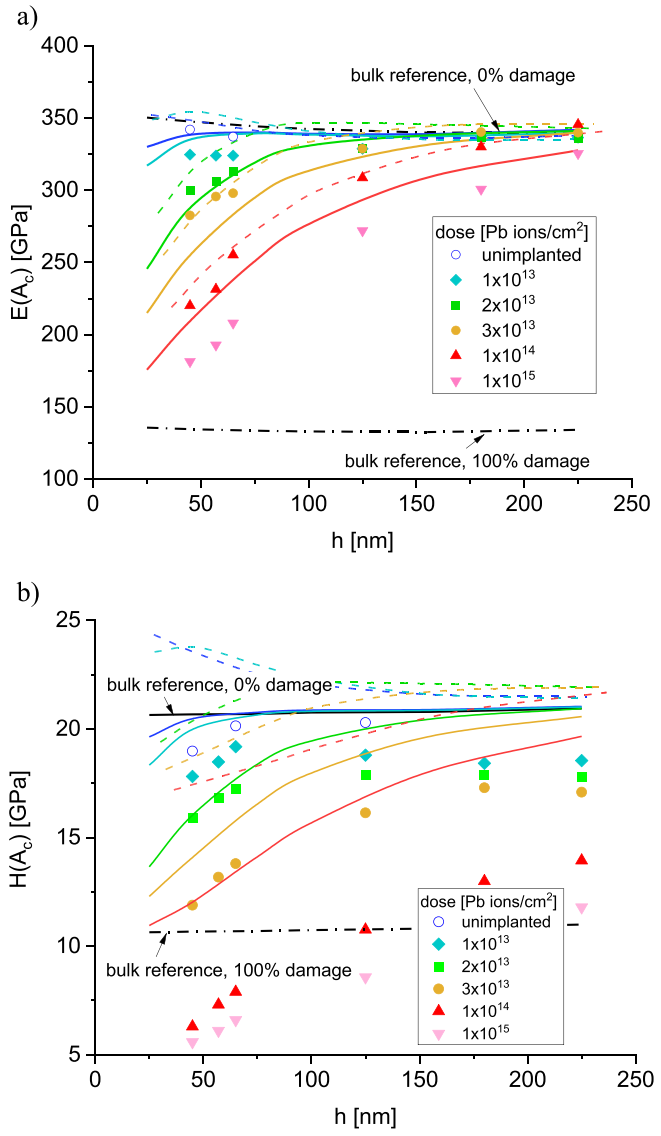

Fig. 3. Comparison of experiments [9] (solid boxes) and simulations without (solid curves) and with residual stress (dashed curves) for (a) Young's modulus $E(A_c)$ and (b) Hardness $H(A_c)$.

stress shifts the predictions by 20 *GPa*($\sim$ 10%) upwards, leading to a very good fit with the measured values.

In contrast, the hardness data show large deviations (Fig. 3b). For the residual stress free simulations, the results are qualitatively comparable for $\leq$ 100 nm up to the dose of $3 \cdot 10^{13}$Pb ions/cm^2. However, for larger depths the experimental data systematically fall below the predicted curves. This seems to originating from two independent effects. Firstly, with increasing depth, the measured hardness should tend to the value of the unimplanted material, which is close to 20 GPa. However, it converges towards a value of only 18 GPa. Because this is not visible in the Young's modulus, it is unlikely that this drop can be attributed to radial cracking. Secondly, the hardness data at high doses drop even below the value of the bulk reference that is predicted for 100% amorphization. This implies that an intense Pb-ion irradiation damages zircon beyond what can be reached by a complete amorphization. This can result from incorporation of additional defect structures that ease plastic deformation. Such defect structures are reported by Zhang et al., who argued that some of the Pb ions might not reside in the zircon lattice at all, but stay in other local domains or nano-clusters newly formed within the crystal [19,20]. Further, Zhang et al. [19] reported an hydrogen enrichment in irradiated zircon, forming OH and/or hydrous species. Beirau et al. already assumed hydrogen to make radiation damaged titanite ($CaTiSiO_5$) more compliant and softer [21]. That this has no obvious effect on the Young's modulus can be explained by the counteracting effect from the growing pile-up in the softened film, see Fig. 2, along with the much larger penetration depth of the elastic strain field, which is therefore less sensitive to variations in the near-surface region.

Considering swelling and compressive residual stresses in the damaged region, the predicted hardness is considerably increased (dashed curves). It is well-known that an in-plane compressive stress increases the measured hardness [22,23]. For an equibiaxial residual stress, which is close to the yield stress, the effect reaches $\geq$ 15% [24]. However, as can be seen from the dashed curves in Fig. 3b), the effect for our simulations is even larger. This could be explained by the clamping of the softer damaged material from all sides. Underneath, the undamaged material represents a harder support and in the lateral direction, the material is pushed against the indenter with maximum compressive stress. It is therefore conceivable that the harder substrate plus an increase of the pile-up enhances the effect of the compressive residual stress on the hardness.

Unexpectedly and in contrast to the Young's modulus, the comparison with the experimental hardness data suggests that the samples do not show any sign of compressive residual stress. At this point it remains unclear, which mechanism could cause the relaxation of the residual stresses. A formation of microcracks should be ineffective, because cracks are closed under compressive residual stresses and, furthermore, under the load of the indenter. The rearrangement of atoms during the amorphization seems to be more reasonable. Such a mechanism could be supported by ongoing ion-irradiation, which allows the damaged material to adjust to the lateral constraint and limit the residual stress to low values, as long as the activation energy is increased. This would be in agreement with the by Zhang et al. [20] assumed strain release in the surface layers.

4. Conclusion

In summary, we successfully implemented depth dependent damage profiles into the model [5] to predict nanoindentation hardness and modulus after extrinsic irradiation. The model serves for validation of the mapping of measured damage profiles into an amorphous phase fraction as function of depth and to study the effect of swelling and residual stress on nanoindentation modulus and hardness data. The extended model provides at least for the Young's modulus a good approximation for the complicated scenario of Pb-implanted natural zircon that includes, e.g., the formation of new phases, phase separation, presence of impurities, hydrogen enrichment and extensive volume expansion. The observed deviations in the hardness behavior of the implanted zircon suggest a surprisingly strong stress relaxation phenomenon, possibly due to irradiation related structural rearrangements. For the depth-damage relationship, SRIM (Stopping and Range of Ions in Matter) code calculated data can also be easily used. The transferability of the model developed for zircon in [5] to pyrochlore, demonstrated in [6], and from intrinsic to extrinsic irradiation damage, shown in this work are very promising conditions and suggest an application of the model also to other types of material and irradiation sources.

Funding

This work was supported by the Deutsche Forschungsgemeinschaft (DFG, German Research Foundation) [grant number BE 5456/2-1].

Declaration of Competing Interest

The authors declare that they have no known competing financial interests or personal relationships that could have appeared to influence the work reported in this paper.

Supplementary materials

Supplementary material associated with this article can be found, in the online version, at doi:10.1016/j.mtla.2022.101506.

References

[1] T.D. de La Rubia, H.M. Zbib, T. Khraishi, B.D. Wirth, M. Victoria, M. Caturla, Multiscale modelling of plastic flow localization in irradiated materials, Nature 406 (2000) 871–874.

[2] K.E. Sickafus, R.W. Grimes, J.A. Valdez, A. Cleave, M. Tang, M. Ishimaru, S.M. Corish, C.R. Stanek, B.P. Uberuaga, Radiation-induced amorphization resistance and radiation tolerance in structurally related oxides, Nat. Mater. 6 (2007) 217–223.

[3] M.I. Dobynde, Y.Y. Shprits, A.Y. Drozdov, J. Hoffman, J. Li, Beating 1 Sievert: Optimal Radiation Shielding of Astronauts on a Mission to Mars, Sp. Weather 19 (2021) 427.

[4] S. Taller, G. VanCoevering, B.D. Wirth, G.S. Was, Predicting structural material degradation in advanced nuclear reactors with ion irradiation, Sci. Rep. 11 (2021) 2949.

[5] N. Huber, T. Beirau, Modelling the effect of intrinsic radiation damage on mechanical properties: The crystalline-to-amorphous transition in zircon, Scr. Mater. 197 (2021) 113789.

[6] T. Beirau, N. Huber, Percolation transitions in pyrochlore: Radiation-damage and thermally induced structural reorganization, Appl. Phys. Lett. 119 (2021) 131905.

[7] N. Huber, T. Beirau, Mechanical Properties of Zircon for Varying Degree of Amorphization Predicted by Finite Element Simulations, TUHH Universitätsbibliothek, 2020.

[8] C. Soyarslan, S. Bargmann, M. Pradas, J. Weissmüller, 3D stochastic bicontinuous microstructures: Generation, topology and elasticity, Acta Mater. 149 (2018) 326–340.

[9] W.C. Oliver, J.C. McCallum, B.C. Chakoumakos, L.A. Boatner, Hardness and elastic modulus of zircon as a function of heavy-particle irradiation dose: II. Pb-ion implantation damage, Radiat. Eff. Defects Solids 132 (1994) 131–141.

[10] W.J. Weber, R.C. Ewing, L.M. Wang, The radiation-induced crystalline-to-amorphous transition in zircon, J. Mater. Res. 9 (1994) 688–698.

[11] J. Lian, S. Ríos, L.A. Boatner, L.M. Wang, R.C. Ewing, Microstructural evolution and nanocrystal formation in Pb + -implanted $ZrSiO_4$ single crystals, Phys. Rev. B 94 (2003) 5695–5703.

[12] N. Huber, W.D. Nix, H. Gao, Identification of elastic-plastic material parameters from pyramidal indentation of thin films, Proc. R. Soc. Lond. A 458 (2002) 1593–1620.

[13] A. Bolshakov, G.M. Pharr, Influences of pileup on the measurement of mechanical properties by load and depth sensing indentation techniques, J. Mater. Res. 13 (1998) 1049–1058.

[14] W.C. Oliver, G.M. Pharr, An improved technique for determining hardness and elastic modulus using load and displacement sensing indentation experiments, J. Mater. Res. 7 (1992) 1564–1583.

[15] Abaqus 3DEXPERIENCEDassault Systèmes, Providence, RI, USA, 2019.

[16] Y. Murakami, K. Tanaka, M. Itokazu, A. Shimamoto, Elastic analysis of triangular pyramidal indentation by the finite-element method and its application to nano-indentation measurement of glasses, Philos. Mag. A 69 (1994) 1131–1153.

[17] K.L. Johnson, Contact Mechanics, Cambridge University Press, 2012.

[18] N. Moharrami, S.J. Bull, A comparison of nanoindentation pile-up in bulk materials and thin films, Thin Solid Films 572 (2014) 189–199.

[19] M. Zhang, L.A. Boatner, E.K.H. Salje, S. Honda, R.C. Ewing, Pb + irradiation of synthetic zircon (ZrSiO4): Infrared spectroscopic investigation, Am. Mineral. 93 (2008) 1418–1423.

[20] M. Zhang, L.A. Boatner, E.K.H. Salje, R.C. Ewing, P. Daniel, W.J. Weber, Y. Zhang, I. Farnan, Micro-Raman and micro-infrared spectroscopic studies of Pb- and Au-irradiated ZrSiO4 : Optical properties, structural damage, and amorphization, Phys. Rev. B 77 (2008) 144110.

[21] T. Beirau, W.D. Nix, R.C. Ewing, G.A. Schneider, L.A. Groat, U. Bismayer, Mechanical properties of natural radiation-damaged titanite and temperature-induced structural reorganization: A nanoindentation and Raman spectroscopic study, Am. Mineral. 101 (2016) 399–406.

[22] T.Y. Tsui, W.C. Oliver, G.M. Pharr, Influences of stress on the measurement of mechanical properties using nanoindentation: Part I. Experimental studies in an aluminum alloy, J. Mater. Res. 11 (1996) 752–759.

[23] Y. Lee, J.Y. Kim, J.S. Lee, K.H. Kim, J.Y. Koo, D. Kwon, Using the instrumented indentation technique for stress characterization of friction stir-welded API X80 steel, Philos. Mag. 86 (2006) 5497–5504.

[24] N. Huber, J. Heerens, On the effect of a general residual stress state on indentation and hardness testing, Acta Mater. 56 (2008) 6205–6213.